ELSEVIER

Contents lists available at ScienceDirect

International Journal of Solids and Structures

journal homepage: www.elsevier.com/locate/ijsolstr





Revealing the unusual rate-dependent mechanical behaviors of nematic liquid crystal elastomers

Christopher Chung ^a, Chaoqian Luo ^a, Christopher M. Yakacki ^a, Bo Song ^b, Kevin Long ^{b,*}, Kai Yu ^{a,*}

- ^a Department of Mechanical Engineering, University of Colorado Denver, Denver, CO 80217, USA
- ^b Materials and Failure Modeling Department, Sandia National Laboratories, Albuquerque, NM 87123, USA

ARTICLE INFO

Keywords: Mesogen rotation Nematic director Mesogen order parameter Liquid crystal elastomers Viscoelasticity Energy dissipation Constitutive modeling

ABSTRACT

Liquid crystal elastomers (LCEs) exhibit unique mechanical properties of soft elasticity and enhanced energy dissipation with rate dependency. They are potentially transformative materials for applications in mechanical impact mitigation and vibration isolation. However, previous studies have primarily focused on the mechanics of LCEs under equilibrium and quasistatic loading conditions. Critical knowledge gaps exist in understanding their rate-dependent behaviors, which are a complex mixture of traditional network viscoelasticity and the soft elastic behaviors with changes in the mesogen orientation and order parameter. Together, these inelastic mechanisms lead to unusual rate-dependent energy absorption responses of LCEs. In this work, we developed a viscoelastic constitutive theory for monodomain nematic LCEs to investigate how multiple underlying sources of inelasticity manifest in the rate-dependent and dissipative behaviors of monodomain LCEs. The theoretical modeling framework combines the neo-classical network theory with evolution rules for the mesogen orientation and order parameter with conventional viscoelasticity. The model is calibrated with uniaxial tension and compression data spanning six decades of strain rates. The established 3D constitutive model enables general loading predictions taking the initial mesogen orientation and order parameter as inputs. Additionally, parametric studies were performed to further understand the rate dependence of monodomain LCEs in relation to their energy absorption characteristics. Based on the parametric studies, particularly loading scenarios are identified as conditions where LCEs outperform conventional elastomers regarding energy absorption.

1. Introduction

Unlike conventional elastomers, liquid crystal elastomers (LCEs) feature rigid mesogens (two or three linked benzene rings (Saed et al., 2016) integrated into their chain backbones, which possess the ability to rotate when subjected to external deformation (Warner and Terentjev, 2007). This rotational behavior of mesogens enables the soft elasticity of LCEs, as evident by a plateau in the stress–strain curves. It also provides an additional mechanism to dissipate energy along with the conventional network viscoelastic relaxation. The inelastic mechanisms within LCE networks lead to an unusual rate dependence and mechanical energy absorption characteristics (Mistry et al., 2021). To date, the remarkable energy absorption and protective capabilities of LCEs have been demonstrated with various proof-of-concept applications, including impact-absorbing helmets, biomedical intervertebral fusion cages, and impact-damping materials (Shaha et al., 2020; Traugutt et al.,

2020).

To accelerate materials design and facilitate the implementation of novel applications of LCEs, it is critical to understand and model the underlying relationships between the mesogen organizations and the unique mechanical behaviors. Extensive research has been conducted to understand these relationships from experimental or theoretical points of view. On the experimental front, investigations have focused on the macroscale rate-dependent stress–strain relationships of LCEs in polydomain or monodomain states (He et al., 2020; Linares et al., 2020; Traugutt et al., 2017; Azoug et al., 2016). The influences of the initial mesogen orientation (i.e., the nematic director) or the degree of mesogen alignment with respect to the stretching directions have also been examined (He et al., 2020; Linares et al., 2020). These studies primarily focused on the mechanical responses at the equilibrium or the quasistatic loading conditions.

At the microscale, wide-angle X-ray scattering (WAXS) is the most

E-mail addresses: knlong@sandia.gov (K. Long), kai.2.yu@ucdenver.edu (K. Yu).

^{*} Corresponding authors.

commonly used technique to characterize the state of the microscale mesogen organizations (Traugutt et al., 2017; Saed et al., 2017; Saed et al., 2017; Murthy and Minor, 1990; Graewert and Svergun, 2013; Harada et al., 2013; Barnes and Verduzco, 2019; Kotikian et al., 2018). However, time is a major limitation of WAXS that the measurements typically require more than five minutes to identify the degree of mesogen alignment. This method restricts the characterizations to the time-independent (i.e., near equilibrium) material behaviors. To this end, polarized Fourier-transform infrared spectroscopy (FTIR) has been used to characterize the macromolecular structure of LCEs (Hanzon et al., 2018; Thomsen et al., 2001; Anglaret et al., 2005; Li et al., 2021; Aksenov et al., 2007; Gharde et al., 2015; Tammer et al., 2005), wherein each FTIR scan can be generated within one second to enable near realtime characterizations. In our recent work, polarized FTIR was adopted in conjunction with in-situ cross-polarized optical measurements to probe the mesogen alignment and reorientation timescale in nematic LCEs coupled with deformation.

For LCE constitutive modeling, the widely recognized Neo-classic theory, developed by Warner and Terentjev (Warner and Terentjev, 2007), is commonly employed to describe the interplay between mesogen orientation and average ordering in the soft elastic responses of monodomain LCEs. Originally, the theory assumes anisotropic random walking of polymer chains to predict the stress-strain relationship in the equilibrium state (Warner et al., 1988; Warner et al., 2003; Bladon et al., 1994; Bladon et al., 1993; Fried and Sellers, 2005; Conti et al., 2002; Conti et al., 2002; Olmsted, 1994; Cesana and Desimone, 2009). Notably, these models did not incorporate the rate-dependency of the mesogen order parameter and nematic director. Continuum theories have been developed to study the coupling effect of viscous director rotation and viscoelastic network deformation. In early viscoelastic models (Terentjev and Warner, 2001; Terentjev et al., 2003; Brand and Pleiner, 1994; Clarke et al., 2001), constitutive equations were derived by applying the variational principle to the Lagrangian function for stored elastic energy and a Rayleigh dissipation function for viscous director rotation and network deformation. Although these models are constrained to small strains and director rotations, they have proven successful in analyzing rate-dependent properties of LCEs. For instance, Terentjev and coworkers (Terentjev and Warner, 2001; Terentjev et al., 2003) proposed an analogous Rayleigh dissipation function to account for entropy production caused by the strain rate and the relative rate of rotation of the director. The resulting constitutive equations were effective in explaining the development of soft elasticity near the nematic-isotropic transition temperature and the power-law stress relaxation behavior.

Recent efforts have extended dissipation principles to consider the effects of large mesogen rotation and large elastic deformation of the anisotropic network (Zhang et al., 2019; Zhu et al., 2011; Wang et al., 2022). Zhang et al. (2019) proposed a Rayleigh dissipation function with a quadratic dependence on the rate of deformation. The model effectively captured various features of the rate-dependent LCE responses, including peak stress and subsequent strain-softening. Notably, since the viscous stress response depends explicitly on the rate of deformation tensor, the model does not exhibit a finite instantaneous stress response as is seen experimentally in stress relaxation tests. In a more recent development, Wang et al. (2022) developed a nonlinear viscoelasticity model that considered both viscoelastic mesogen rotation and chain relaxation. The network deformation and free energy were decomposed into elastic and viscous parts, and a constitutive equation for the objective rate of director rotation was derived. However, the model cannot reproduce the initial anisotropy of modulus in nematic LCEs. Additionally, the constitutive modeling assumed a constant value for the mesogen alignment degree, with the timescales of mesogen rotation determined by fitting stress-strain curves of monodomain LCE samples deformed in the perpendicular direction to the initial nematic director.

Despite these pioneering studies, critical knowledge gaps remain in the field, specifically to fully understand the rate-dependent mechanical responses of LCEs. First, the timescales for mesogen alignment and rotation are usually empirically fit. It is desirable to experimentally probe these timescales and reveal their relationships with mechanical responses in a rigorously defined thermodynamics modeling framework, especially when the LCE mechanical behaviors depend on various material and process parameters. Second, potential applications of LCEs involve intermediate or dynamic loading. However, to the best of our knowledge, existing studies on the viscoelastic behaviors of LCEs are limited to the quasi-static loading rates (far below 1 s $^{-1}$) that are slower than strain rates anticipated in transient mechanical applications. Third, existing studies primarily focus on stress–strain relationships and the soft elasticity of LCEs. How the background polymer network relaxation and mesogen rotation independently contribute to the energy absorption characteristics remain unclear.

In this study, we develop a viscoelastic constitutive model for monodomain nematic LCEs that incorporates the evolution of the nematic director and mesogen alignment degree during the network deformation and use the model to study the mechanical responses and energy dissipation of LCEs across a broad spectrum of loading rates, from quasistatic to dynamic. Previous studies have demonstrated that when monodomain LCEs are subjected to loading at an oblique direction of their initial nematic director, they could exhibit some unique mesogen microstructures, such as stripe domains (Zhang et al., 2020; Verwey et al., 1996; Zubarev et al., 1999) or potential domain-domain interactions. In this study, instead of delving into the formation and evolutions of such mesogen structures at the microscale, we adopt a continuum-level mechanics modeling approach to formulate the relationships between the average mesogen orientation and the macroscopic stress-strain behavior. The modeling domain encompasses a volume size that is wellabove the dimensions of the aforementioned mesogen microstructures. By adopting this approach, we will be able to effectively formulate the rate-dependent mechanical responses of monodomain LCEs, reveal the underlying energy dissipation mechanisms, and assist in the design of macroscopic protective devices.

The modeling framework in this study combines the neo-classic LCE theory for mesogen interactions and rheological modeling components for the background viscoelasticity of the amorphous network. The nematic director and order parameter are treated as internal variables. Their relaxation times scale with macroscope deformation and are experimentally determined using FTIR measurements. The ratedependent evolution rules for mesogen rotation, alignment, and network viscoelastic relaxation are rigorously derived based on the thermodynamics energy inequality law. The model is shown to capture the uniaxial tension and compression behaviors of LCEs with different initial nematic director orientations across six decades of strain rate (0.01–1600 s⁻¹). After verification, the model performed parametric studies to reveal the soft elastic mechanisms of LCEs, as well as contributions of mesogen rotation and viscoelastic network relaxations on the overall energy absorption capabilities. The parametric studies consider operational parameters, such as the initial nematic director, the loading rate, and the terminal strain. The presented study provides valuable insights for rational designs of material structures and operational conditions of LCEs for various applications as energy-absorbing materials.

2. Materials and experimental methods

2.1. Preparations of LCE samples

This study employs a main chain nematic LCE as the tested material. Thin-film LCE samples were prepared for uniaxial tension tests. They were synthesized using a two-stage thiol-acrylate Michael addition polymerization developed by (Saed et al., 2016), as shown in Fig. 1. The first stage prepared polydomain LCE samples, which were later processed in a second-stage cure to produce a monodomain sample. 21.5 g (36.5 mmol) diacrylate mesogens 1,4-Bis-[4-(3-acryloyloxypropyloxy)

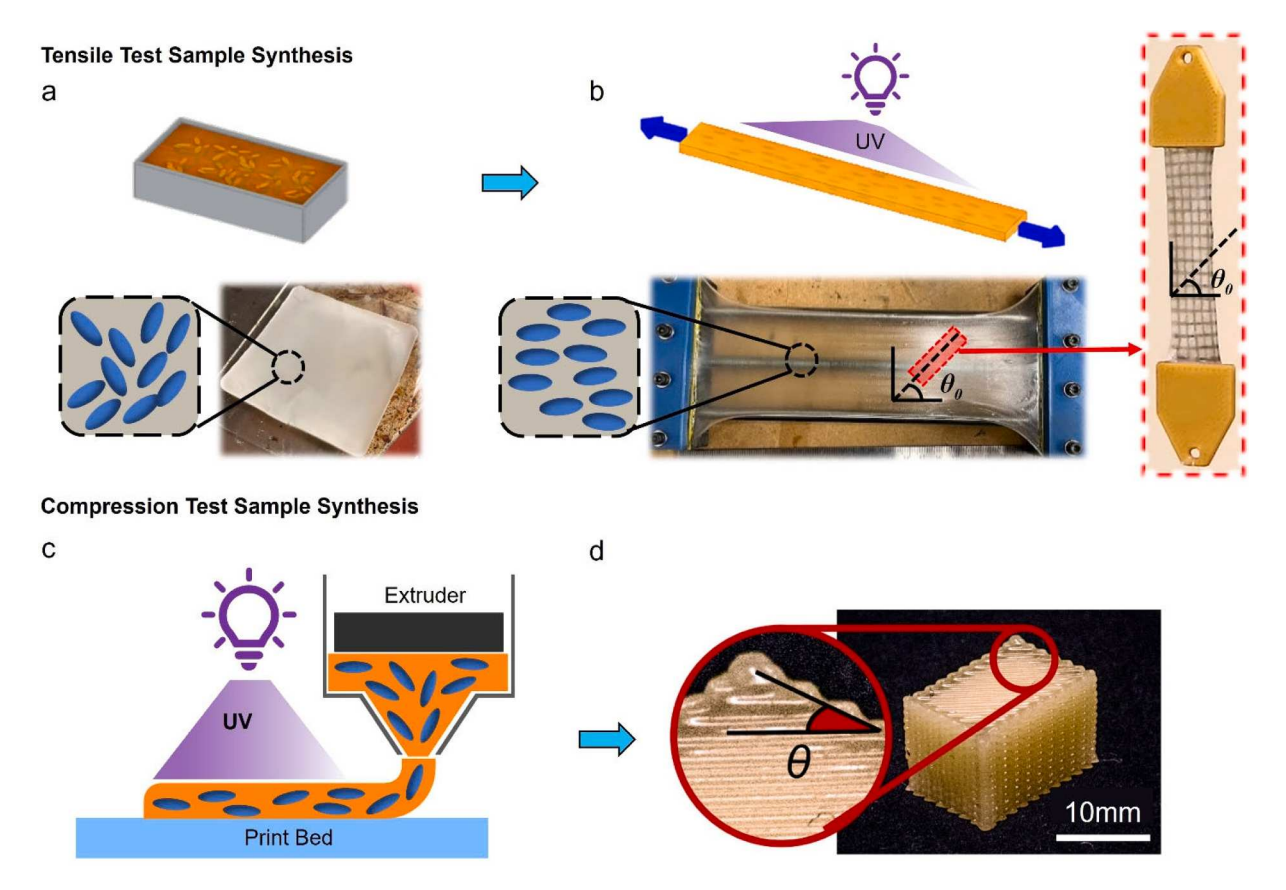


Fig. 1. Schematic view showing the sample preparation processes. (a) RM257 and toluene are mixed in a flask and heated to 85 °C. The rest of the chemicals are vigorously mixed in, degassed, then poured into a mold. (b) After 24 h at room temperature and 12 h at 85 °C, the resultant polydomain LCE is stretched and exposed to UV light for 30 min on each side. Samples are then cut according to specific initial nematic director orientations. (c) Schematic view of the DIW extrusion process to print monodomain LCEs. (d) Resultant monodomain LCE samples (Mistry et al., 2021).

benzoyloxy]-2-methylbenzene (RM257) were first dissolved in 6.7 g toluene at 85 °C. After the solution was cooled to room temperature, 5.2 g (28.3 mmol) di-thiol spacer 2,2'-(ethylenedioxy) diethanethiol (EDDET), 0.13 g (0.58 mmol) photo-initiator 2-hydroxy-4'-(2-hydroxyethoxy)-2-methylpropiophenone (HHMP), 1.0 g (2.1 mmol) crosslinker pentaerythritol tetrakis (3-mercaptopropionate) (PETMP), and 0.22 g (2.1 mmol) catalyst triethylamine (TEA) were vigorously mixed in. The solution was degassed and poured into a 1.25 mm-deep mold in a light-absent environment for 24 h at room temperature. After the solution was cured, it was then placed into a vacuum oven at 85 °C to evaporate residual toluene. After 12 h, a loosely crosslinking polydomain LCE was obtained. For the chemical precursors mentioned above, RM257 was purchased from Wilshire Technologies (Princeton, NJ, USA), and the rest of the chemicals were purchased from Sigma-Aldrich (St. Louis, MO, USA) without further purification.

The second stage of curing transformed the synthesized polydomain LCE into a monodomain LCE. The polydomain sample was stretched homogenously at 125 % strain to ensure alignment of the liquid crystals parallel to the stretching direction. While the samples were clamped, they underwent crosslinking in a UV chamber (UVP, Ultraviolet Crosslinkers, Upland, CA, USA) for 30 min on each side to ensure a homogeneous photopolymerization. Samples were then cut in known directions with respect to the nematic director (or the directional vector of the mesogens), with $\theta_0=0^\circ,\,30^\circ,\,45^\circ,\,60^\circ,\,$ and $90^\circ.$ Each specimen was cut with a length of 60 mm, width of 10 mm, and thickness of 0.8 mm. The samples were then stamped with a 2 mm by 2 mm grid to track the degree of shear deformation under the uniaxial tension condition.

Creating a monodomain bulk cubic sample for compression tests is challenging with the aforementioned two-step programming method. This is because the UV light cure could not fully penetrate deep within

the sample to generate a uniform curing degree and mesogen organizations. To this end, we synthesized the cubic monodomain compression samples $(5\times5\times5\,\text{mm}^3)$ using a direct-ink-writing (DIW) approach. The above-mentioned precursor monomers and stoichiometry for acrylate-thiol functional groups were preserved. After mixing all the materials, they were first loaded into the DIW printing barrel and left in an oven at 70oC for half an hour to partially cure the resin into a suitable viscosity via a Michael-addition reaction. During the DIW printing, mesogens were aligned in the printing directions due to the shear stress involved in the viscous flow of the ink in the fine nozzle (0.5 mm diameter). The printed LCE filament was exposed to UV light from LEDs surrounding the nozzle. After printing, the LCE samples were fully cured through exposure to high-intensity UV light for 2 h. Detailed printing setup and processing parameters can be found in our recent study (Mistry et al., 2021).

In the Supplementary Materials (Section S1), the mechanical properties between molded LCE samples and DIW printed samples are compared using uniaxial tension tests. Specifically, monodomain LCE samples were printed in different directions (0, 45, and 90 degrees) with respect to the longitudinal direction. These samples had identical geometry to the molded samples (60 mm in length, 10 mm in width, and 0.8 mm in thickness) and were tested under quasistatic tensile loading conditions. The results suggest that the mechanical properties of molded LCE samples and DIW printed samples were very similar to each other. Therefore, they can be studied using the same modeling framework and the same set of model parameters.

2.2. Polarized FTIR characterizations

Polarized FTIR tests were used to evaluate the mesogen order

parameter and nematic director orientation as the LCEs were stretched. The FTIR characterizations were performed at room temperature on a Nicolet 6700 FTIR spectrometer (Thermo Scientific, Waltham, MA, USA) with a KRS-5 wire grid polarizer and a custom-built sample holder. The LCE sample with a dimension of 16.5 mm \times 3.9 mm \times 0.45 mm was exposed to polarized infrared light. The FTIR traces were collected in different stretch directions by averaging 32 scans of the signal at a resolution of 2 cm $^{-1}$.

As shown in Fig. 2a, LCE samples are exposed to polarized light during the tests. Chemical bonds (e.g., mesogens) on the chain backbone have the strongest light absorption when the nematic director is parallel to the polarizer and the weakest absorption when perpendicular. Their alignment degree can be identified by comparing the absorption peaks at different irradiation directions. Fig. 2b shows the absorption spectrum of the stretched LCE samples. The peak areas of the C-S bond in the parallel and perpendicular directions of stretch are used to calculate the dichroic ratio of the anisotropic LCE network: $D = A_{max}/A_{min}$, where A_{max} is the maximum absorbance in the parallel direction, and A_{\min} is the minimum absorbance in the perpendicular direction (Fig. 2c). As adopted in the previous study, the order parameter *S* is related to the dichroic ratio as: S = (D-1)/(D+2). Note that this scaling relationship ensures a welldefined mathematical range of the order parameter, S. For LCEs in the polydomain state or isotropic state without macroscopic mesogen alignment, the FTIR absorption peaks will be near identical in all directions. Therefore, D = 1 and S = 0. For the case of monodomain LCEs with a perfect alignment of mesogens, A_{min} would approach zero and Dapproaches infinite, which leads to S = 1.

2.3. Uniaxial tension tests at quasi-static loading rates

An Insight 30EL (MTS, Eden Prairie, MN, USA) with a 500 N load cell was used for all tensile tests at quasi-static loading rates. Significant

shear deformation was developed due to the internal mesogen rotation for LCE samples with mesogen alignment in an oblique direction relative to tension. To allow free rotation of LCE samples at each end, the LCE samples were first glued to rigid PLA endplates and then fixed to the clamps via fishing wires, as shown in Fig. 3. This characterization approach was recently developed by He et al. and adopted in this study (He et al., 2020). Once the LCE samples were in place, three tensile strain rates, 0.01, 0.05, and 0.1 s⁻¹, were tested for each θ_0 at room temperature.

Readers should note that when the LCE samples are stretched in the oblique direction, they exhibit significant shear deformation. Although the adopted fixture allows the rotation of the clamps, notable boundary effects are observed near the top and bottom clamps. As shown in Fig. 3, the deformation of the gridlines near these clamps differs noticeably from that in the central region of the sample. To ensure a reliable measurement of strain, we focus on the central region of the sample for strain measurement. Specifically, during each tension test, the shear deformation was recorded by tracking the grid lines at the central portion of the LCE sample with a relatively uniform strain field. The DSLR camera (Canon EOS 80D) was placed on a tripod perpendicular to each sample recording a video. The video frames were then processed through MATLAB and ImageJ to extract the shear angle, α .

2.4. Uniaxial compression tests at quasi-static and dynamic loading rates

The uniaxial compression behaviors of LCE samples were tested across five decades of strain rate (from $0.01~\rm s^{-1}$ to $1600~\rm s^{-1}$). The quasistatic uniaxial compression tests were performed using the MTS tester. Samples were subject to a minimum of 0.5 nominal strain at each condition for comparison with quasi-static experiments. At the dynamic loading rates, Kolsky bar compression tests were used to measure the mechanical responses of the LCE. During the tests, LCE specimens were

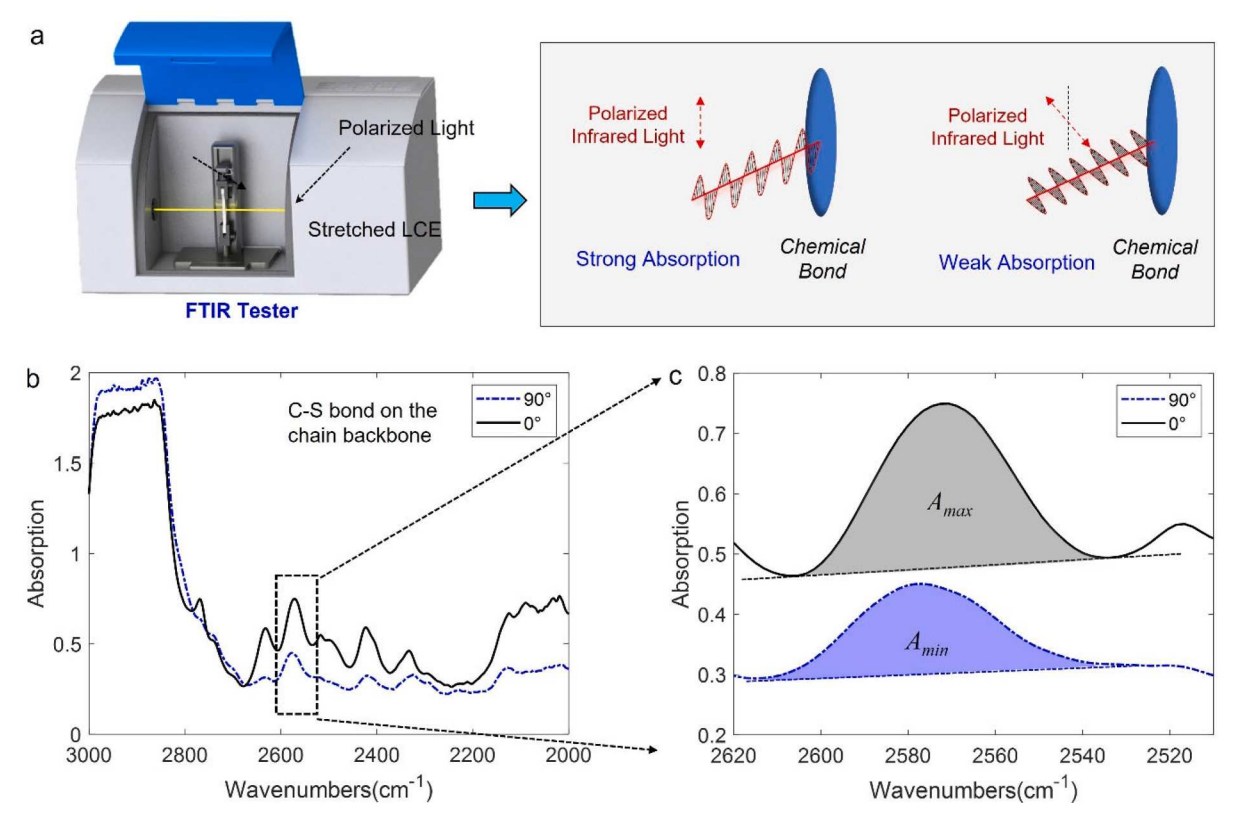


Fig. 2. (a) Schematic view of the polarized FTIR characterizations and working mechanism. (b) The FTIR absorption spectrum of the stretched LCE samples. The light polarization is first parallel and then perpendicular to the sample stretching direction. (c) The absorption peak areas of the C-S bonds in the parallel and perpendicular stretch directions.

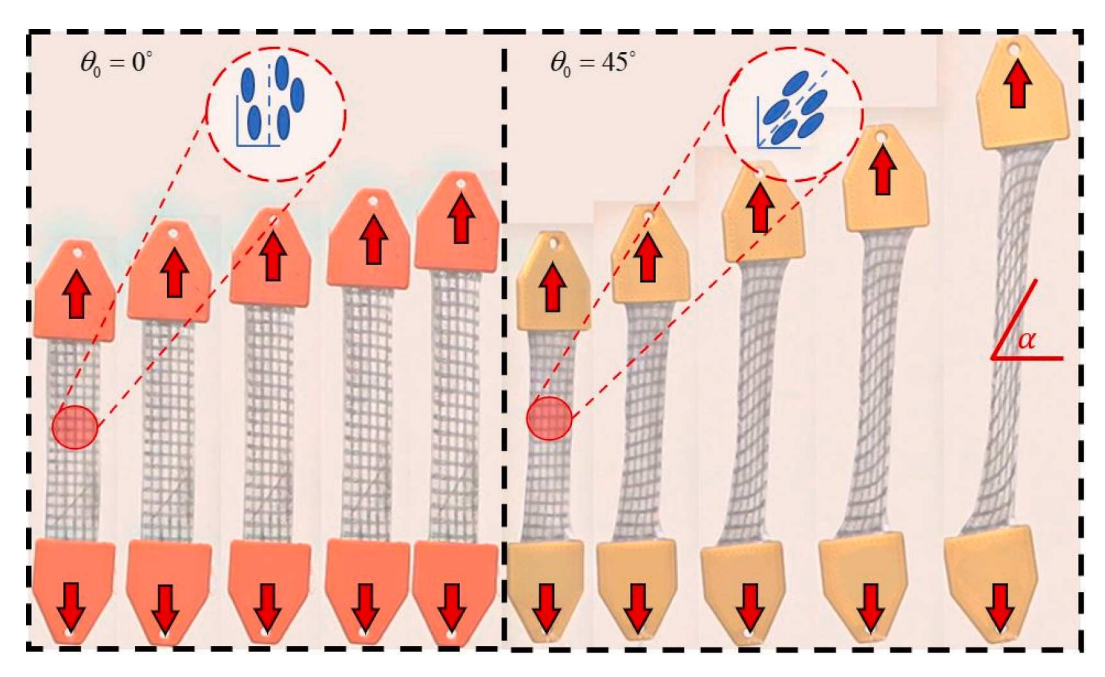


Fig. 3. Two of our monodomain LCE samples were used during our tension test. The left sample is with the nematic director oriented in the direction of tension, $\theta_0 = 0^{\circ}$, while the right sample is initially oriented at $\theta_0 = 45^{\circ}$. The first sample does not exhibit notable shear deformation with increasing tension, while the second sample displays very strong shearing. We isolated our measurements for the shear angle, α , to the center of the sample to reduce any edge effects.

sandwiched between the incident and transmission bars in a stress-free state prior to the start of the experiment. These experiments were carried out at nominal strain rates of $800 \, \text{s}^{-1}$ and $1600 \, \text{s}^{-1}$, which of the corresponding data and experimental methods previously documented (Tammer et al., 2005).

3. Constitutive modeling

3.1. Overview of the modeling framework

The overall modeling framework is illustrated in Fig. 4. It consists of two parts. The first part (left branch) is the neo-classical branch describing the effect of mesogen organization on the network elasticity. The nematic director and mesogen order parameter are characterized by a vector and a scalar, respectively, which are taken to be state variables in the constitutive modeling (Warner and Terentjev, 2007). We note that these two quantities evolve with the external loading of LCEs, and their evolution rules are developed in this study for the first time using quantifiable methods. The second part of the model is the multibranched viscoelastic Maxwell model representing the background network viscoelasticity (Christensen et al., 2012). Each branch has a

unique dashpot relaxation time to represent the diverse relaxation timescales of polymer chains within the amorphous network.

3.2. The neo-classical branch

Following Warner and Terentjev (2007), the neo-classical free energy of incompressible nematic LCE networks is given by:

$$\varphi_{nc} = \frac{\mu_{nc}}{2} \left[tr(\mathbf{A}^{-1} \mathbf{F} \mathbf{A} \cdot \mathbf{F}^T) - ln(det(\mathbf{A}^{-1} \mathbf{F} \mathbf{A} \cdot \mathbf{F}^T)) - 3 \right], \tag{1}$$

where F is the deformation gradient tensor and μ_{nc} is the shear modulus. A is the anisotropic conformational tensor that maps the current configuration nematic director scaled by the current nematic order parameter to the deformation gradient tensor, and A_{\circ} is identical but instead maps the reference configuration. They are respectively related to the initial nematic director n_{\circ} (a unit vector along the direction of mesogen alignment) and current nematic director n as:

$$A = I + 3S\left(n \otimes n - \frac{1}{3}I\right) \tag{2a}$$

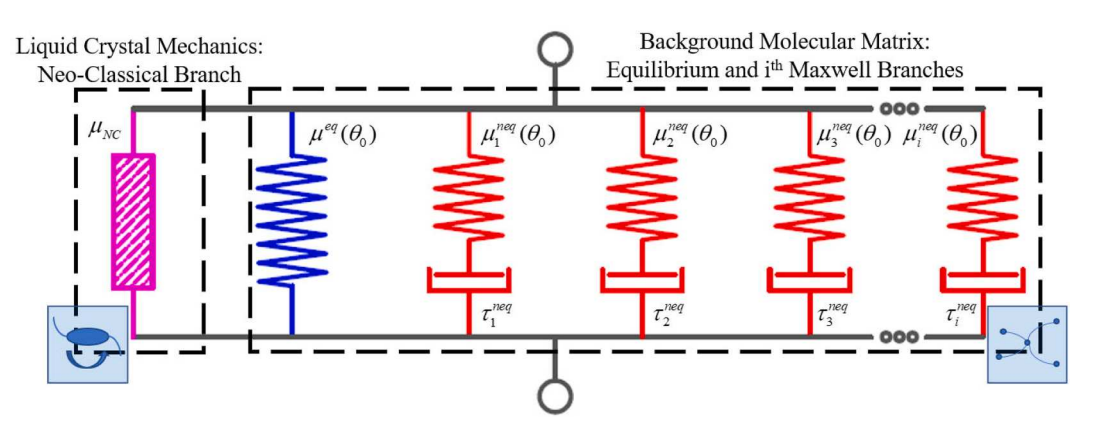


Fig. 4. The rheological diagram above represents the inner workings of our constitutive model.

$$A_* = I + 3S_* \left(n_* \otimes n_* - \frac{1}{3}I \right), \tag{2b}$$

with I being the second-order identity tensor. S is the mesogen order parameter. For LCEs with mesogens perfectly aligned, S=1. For LCEs without mesogen alignment (the isotropic state), S=0. However, it should be noted S=0 presents an instability outlined by Warner and Terentjev (2007) and is avoided in our formulation.

The neo-classical branch reflects the anisotropy resulting from the ordered nematic domains. However, unlike conventional anisotropy, the constitutive relationships of LCEs are dynamic relative to the nematic director orientation and reorientation of these nematic domains. Therefore, the existence of A and A⁺ transforms the well-known neo-Hookean model into the neo-classical model presented. As the model begins with a strain energy density, it is a hyperelastic model that requires a separate definition for the time evolution of the internal state variables of n and S. Previously, the definitions of n and S have reflected near-equilibrium behaviors. Section 3.4 will define the explicit evolution rules of n and S, which amend the neo-classical model to a rate-dependent constitutive relation.

3.3. The multi-branched viscoelasticity branches

The viscoelasticity of the background amorphous network is modeled by a multi-branched Maxwell model, which is comprised of an equilibrium and several non-equilibrium branches of Maxwell elements. The stress–strain relationship of the equilibrium branch follows the neo-Hookean model for hyperelastic materials. For the i^{th} non-equilibrium branch, the total deformation gradient is decomposed into an elastic and viscous part: $F_i = F_i^* F_i^*$. The total free energy is

$$\varphi_{vis} = \varphi^{eq} + \sum_{i=1} \varphi_i^{neq} = \frac{\mu^{eq}}{2} tr(\mathbf{F}^e \mathbf{F}^{eT} - \mathbf{I}) + \sum_{i=1} \frac{\mu_i^{neq}}{2} tr(\mathbf{F}_i^e \mathbf{F}_i^{eT} - \mathbf{I}), \tag{3}$$

where μ^{eq} and μ^{neq}_i are the equilibrium shear modulus and non-equilibrium shear moduli of the i^{th} Maxwell branches, respectively.

Monodomain LCEs exhibit transversely isotropic behaviors. The material properties strongly depend on the direction of external loading with respect to the initial orientation of mesogen alignment. When the LCE networks are deformed, the mesogens tend to reorient towards the direction of the largest principal stretch, which represents an energy minimizing configuration (Wang et al., 2022). Based on this consideration, we formulate the shear moduli of the multi-branched model as a function of the directional angle between the initial nematic director and the direction of the largest principal stretch in the reference configuration, θ_0 . Specifically, if we consider the uniaxial deformation of the monodomain LCEs, where mesogen reorientation occurs within the 2D plane, we have:

$$\mu^{eq}(\theta_0) = \mu_\perp^{eq} + \left(\mu_\parallel^{eq} - \mu_\perp^{eq}\right) f(\theta_0), \tag{4a}$$

and

$$\mu_i^{neq}(\theta_0) = \mu_{i\perp}^{neq} + (\mu_{i\parallel}^{neq} - \mu_{i\perp}^{neq}) f(\theta_0), \tag{4b}$$

where μ_{\perp}^{eq} and $\mu_{i\perp}^{neq}$ are the equilibrium and viscous shear moduli when the sample's nematic director is perpendicular to the applied stress. μ_{\parallel}^{eq} and $\mu_{i\parallel}^{neq}$ are the same shear moduli when the applied stress is parallel to the nematic director. The directional moduli in Eq. (4a) and Eq. (4b) resemble the conventional rule of mixtures in composite lamina theories (Tsai and Hahn, 2018), wherein the shear moduli of monodomain LCEs rely on the loading direction and the amount of stress shared between the mesogens and the background molecular matrix. However, unlike the conventional expressions, the moduli between the two extreme loading cases depend on the mesogen directional angle in a nonlinear manner. The detailed expression of the mapping function, $f(\theta_0)$, will be

determined from experiments as shown in the following section.

3.4. System free energy and stress-strain relationships

The total system Helmholtz free energy density of LCE networks is the summation of the neo-classical and viscoelastic contributions:

$$\varphi = \varphi_{nc} + \varphi_{vis}. \tag{5}$$

Note that in addition to the deformation, the system free energy depends on the mesogen alignment degree S, the nematic director n, and the viscoelastic state variables. For an isothermal process, the Clausius-Duhem form of the Second Law of thermodynamics with this Helmholtz free energy density becomes (Holzapfel, 2002):

$$\boldsymbol{\tau} : \boldsymbol{D} - \dot{\boldsymbol{\varphi}} = \left(\boldsymbol{\sigma} - \frac{\partial \varphi_{nc}}{\partial \boldsymbol{F}} \boldsymbol{F}^{T} - \frac{\partial \varphi^{eq}}{\partial \boldsymbol{F}} \boldsymbol{F}^{T} - \sum_{i=1}^{n} \frac{\partial \varphi_{i}^{neq}}{\partial \boldsymbol{F}_{i}^{e}} \boldsymbol{F}_{i}^{eT}\right) : \boldsymbol{D} + \sum_{i=1}^{n} \left(\boldsymbol{\sigma}_{i}^{neq}\right) : L_{v}\left(\boldsymbol{b}_{i}^{e}\right) \cdot \boldsymbol{b}_{i}^{e} - \frac{\partial \varphi}{\partial \boldsymbol{n}} \dot{\boldsymbol{n}} - \frac{\partial \varphi}{\partial \boldsymbol{S}} \dot{\boldsymbol{S}} \geqslant 0,$$

$$(6)$$

where D is the rate of deformation tensor, and $D = \left(\dot{F}F^{-1} + F^{-T}\dot{F}^{T}\right)/2$. $L_{\nu}(b_{i}^{e})$ stands for the material time derivative of the left Cauchy-Green deformation tensor b_{i}^{e} of the i^{th} non-equilibrium branch.

On the right side of Eq. (6), the first two terms relate to the Cauchy stress in the equilibrium and non-equilibrium branches (σ_i^{eq} and σ_i^{neq}), respectively. To ensure the inequality holds for arbitrary evolutions of the state variables and/or rate of deformation, the Coleman and Noll procedure is followed, and the Cauchy stress of the LCE is identified as

$$\boldsymbol{\sigma} = \boldsymbol{\sigma}_{nc} + \boldsymbol{\sigma}^{eq} + \sum_{i=1}^{n} \boldsymbol{\sigma}_{i}^{neq} = \frac{\partial \varphi_{nc}}{\partial \boldsymbol{F}} \boldsymbol{F}^{T} + \frac{\partial \varphi^{eq}}{\partial \boldsymbol{F}} \boldsymbol{F}^{T} + \sum_{i=1}^{n} \frac{\partial \varphi_{i}^{neq}}{\partial \boldsymbol{F}_{i}^{e}} \boldsymbol{F}_{i}^{eT},$$

$$= \mu_{nc} \boldsymbol{A}^{-1} \boldsymbol{F} \boldsymbol{A} \cdot \boldsymbol{F}^{T} + \mu^{eq} \boldsymbol{F} \boldsymbol{F}^{T} + \sum_{i=1}^{n} \mu_{i}^{neq} \boldsymbol{F}_{i}^{e} \boldsymbol{F}_{i}^{eT} - p \boldsymbol{I}$$

$$(7)$$

where p is the *undetermined* pressure to be determined by the boundary conditions and the incompressibility model idealization. The derivation for Cauchy Stress from the free energy density function can be seen in Supplementary Materials (Section S2).

The following viscous flow rule is adopted for the non-equilibrium branches to guarantee the dissipation inequality satisfied in the second term of Eq. (6) independent of any other thermodynamic or internal state variable evolution:

$$L_{v}(\boldsymbol{b}_{i}^{e})\cdot\boldsymbol{b}_{i}^{e}=\boldsymbol{\Pi}_{i}:\boldsymbol{\sigma}_{i}^{neq},\tag{8a}$$

where Π_i is the fourth order relaxation time tensor of the i^{th} non-equilibrium branch, which can be defined as (Reese and Govindjee, 1998):

$$\mathbf{\Pi}_{i} = -\frac{1}{\eta_{i}} (\mathbf{I}_{4} - \frac{1}{3} \mathbf{I} \otimes \mathbf{I})$$
(8b)

where I_4 is the fourth-order identity tensor, and η_i is the viscosity of the i^{th} non-equilibrium branch. η_i can be related to the characteristic relaxation time τ_i^{neq} for the background polymer network and shear modulus μ_i^{neq} in Eq. (4b) as: $\eta_i = \tau_i^{neq} \mu_i^{neq}$. Note that τ_i is a constant for a given branch at room temperature.

Like the definition of the viscous flow rule, the evolution of order parameter S and nematic director n are proposed based on two scalar relaxation times, τ_n and τ_S . τ_n is the characteristic relaxation time for mesogen rotation, and τ_S is the characteristic relaxation time for chain ordering. As the specimens undergo external loading, the mesogens will rotate and align toward the maximum tensile principal strain. The change in the nematic director, \vec{n} , is directly related to the change in free energy density seen in Eq. (3).

$$\dot{\mathbf{n}} = \mathbf{W}\mathbf{n} - \frac{1}{\tau_n \varphi} (\mathbf{I} - \mathbf{n} \otimes \mathbf{n}) \frac{\partial \varphi}{\partial \mathbf{n}},\tag{9a}$$

with

$$\frac{\partial \varphi}{\partial \boldsymbol{n}} = \frac{-3\mu_{nc}S}{(1-S)(1+2S)} \boldsymbol{F} \boldsymbol{A}_* \boldsymbol{F}^T \boldsymbol{n}^T$$
(9b)

where W is the spin tensor for rigid-body rotation: $W=1/2\left(\dot{F}F^{-1}-F^{-T}\dot{F}^{T}\right)$ and τ_{n} is an experimentally fitted time constant for the rotation of the nematic director. The change in the nematic order parameter, \dot{S} , is related to the change in free energy density due to the change in the nematic order parameter.

$$\dot{S} = -\frac{1}{\tau_5 \varphi} \frac{\partial \varphi}{\partial S},\tag{10a}$$

with

$$\frac{\partial \varphi}{\partial S} = \frac{\mu_{nc}}{2tr(\mathbf{F}\mathbf{A}_*\mathbf{F}^T)(1-S)^2} - \frac{\mu_{nc}(6S^2+3)\mathbf{n}\mathbf{F}\mathbf{A}_*\mathbf{F}^T\mathbf{n}^T}{2(1-S)^2(1+2S)^2} - \frac{\mu_{nc}}{(1-S_*)(1+2S_*)}$$
(10b)

where τ_S is the relaxation time for the change in mesogen order parameter, which depends on the macroscopic deformation as described below. Detailed derivations on Eq. (9b) and (10b) are shown in Supplementary Materials (Section S3).

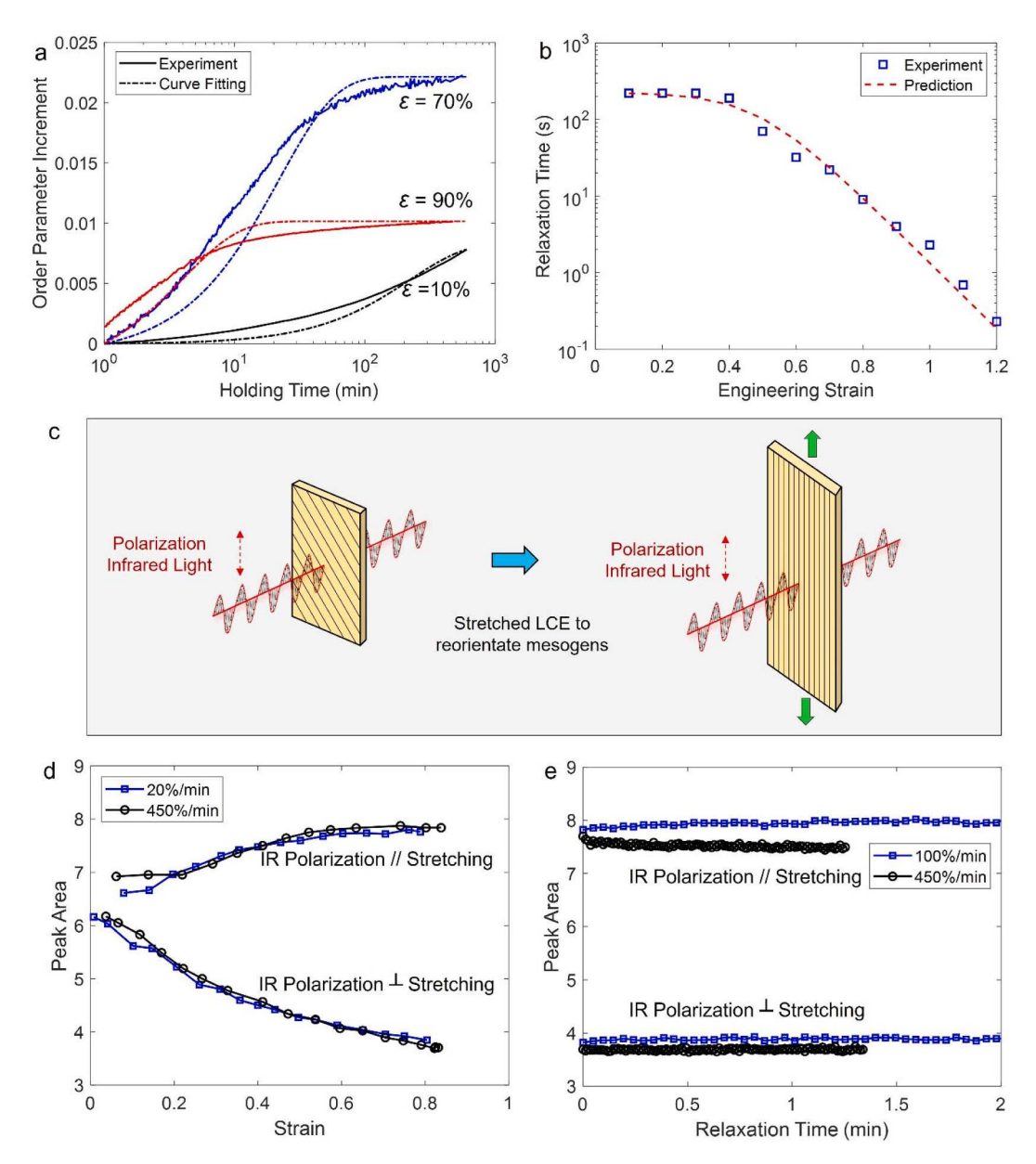


Fig. 5. Polarized FTIR measurements to determine nematic director rotation and reorientation time scales. (a) Increment of mesogen order parameter during the stabilization period at 10%, 70%, and 90%, and associated model fits. (b) The relaxation times of the mesogen order parameter plotted as a function of strain. (c) Experimental setup when using FTIR to determine the nematic director reorientation time scale. (d) The evolution of absorption peak area during the FTIR measurements, wherein the LCE samples are continuously stretched at different loading rates. (e) The absorption peak area during the FTIR measurements when the LCE samples are at the holding step.

4. Results and discussion

4.1. Polarized FTIR to determine the time scales for mesogen alignment and rotation

The timescales for mesogen alignment, τ_S , and nematic director reorientation, τ_n , are determined primarily using the polarized FTIR measurements following a procedure developed by Luo et al. (Luo et al., 2021). The detailed working mechanisms are also described in Section 2.2. To determine the τ_S ; polydomain LCE samples were subject to the stepped-loading condition. The sample was stretched by 10 % engineering strain within one second and then stabilized for 10 mins to reach a near-equilibrium state, wherein mesogens gradually aligned with increased order parameter. After that, the sample was stretched by another 10 % to reach the next strain level. Fig. 5a shows the evolution of the order parameter when the strain level is 10 %, 70 %, and 90 %, respectively. The evolutions of the order parameter at other strain levels are shown in the Supplementary Materials (Section S4). Note the net changes in order parameter at different strain levels are different. By fitting the experimental data using an exponential equation (dashed lines in Fig. 5a), the relaxation time τ_S at a specific strain level can be determined (Fig. 5b). It is observed that the relaxation time is nearly a constant $\sim\!220$ s when the strain is below 40 % and then starts to decrease dramatically. Mathematically, the relationship between τ_S and strain levels can be regressed using the following empirical equation:

$$\tau_S(\varepsilon) = \frac{\gamma_0}{\gamma_1 + e^{\gamma_5 \varepsilon}},\tag{11}$$

where $\gamma_0 = 2.7 \times 10^4$, $\gamma_1 = 120.8$, and $\gamma_2 = 9.91$. Note that ε denotes the tensile strain in the uniaxial loading experiments. For general 3D loading conditions, ε is the maximum principal tensile strain.

FTIR characterizations were performed on monodomain LCE samples with an oblique nematic director (30°) to examine the nematic director reorientation kinetics, τ_n . During the tests, the polarization direction of incident infrared light was fixed either normal or parallel to the stretching direction of LCE samples (Fig. 5c). When the LCE samples were continuously stretched, mesogens and other functional groups on the chain backbone gradually aligned in the same direction. This alignment led to an increased absorption peak in the parallel direction and decreased absorption peak in the normal direction. The sample was stretched continuously at 20 %/min and 450 %/min to 80 % engineering strain during our tests. After reaching \sim 80 %, the sample was stabilized for \sim 2 min with a fixed strain level.

The evolutions of peak areas in the parallel and perpendicular directions of tension during the loading step and holding step are respectively shown in Fig. 5d and Fig. 5e. It is observed that the difference in the peak area evolutions at different loading rates is less significant, and the peak area remained constant over the entire period of the holding step. The FTIR characterization results suggest that the reorientation rate of the nematic director in the monodomain LCE network is faster than the selected loading rates. At the highest loading rate of 450 %/min, the LCE sample was stretched to \sim 0.8 engineering strain within ~ 13.3 s. Therefore, the timescale for the nematic director orientation is estimated to be below 13.3 s. It is important to note that, due to limitations in the experimental fixture, we were unable to further increase the loading rate on the samples. Therefore, we can only obtain the range of $\tau_n \leq 13.3$ s from the FTIR experimental characterization. However, this estimation provides important information for determining the value of τ_n through curve fitting. A previous study by Zhang et al. (2019) reveals that the characteristic timescale for the director rotation is approximately 0.01 s. Incorporating this previous study, we set the initial guess for τ_n to be within the range of [0.01 s-13.3 s] during the curve fitting process. This consideration is particularly important when the developed modeling framework involves many parameters.

4.2. Quasi-static uniaxial tension behavior

The established modeling framework was first applied to study uniaxial tension of the monodomain LCEs with different initial nematic directors ($\theta_0=0^\circ, 30^\circ, 45^\circ, 60^\circ, \text{and } 90^\circ)$ and different engineering strain rates (0.01, 0.05, and 0.1 s⁻¹). In the Supplementary Materials (Section S5), a schematic view is presented that shows the top view and side view of the LCE sample during the deformation. When the LCE sample is subjected to uniaxial tension in X_2 direction, the displacement u_1 only depends on x_1 the adopted experimental fixture prevents rigid body rotation within the X_1 - X_2 plane (see Fig. 1). In addition, u_2 depends on both x_1 and x_2 , and u_3 only depends on x_3 . As a result, the non-zero components of the deformation gradient tensor are $F_{11}=\partial u_1/\partial x_1$, $F_{21}=\partial u_2/\partial x_1$, $F_{22}=\partial u_2/\partial x_2$, and $F_{33}=\partial u_3/\partial x_3$. Notably, the tensor component $F_{12}=\partial u_1/\partial x_2$ is determined to be zero. The global deformation gradient is:

$$\mathbf{F} = \begin{pmatrix} F_{11} & 0 & 0 \\ F_{21} & F_{22} & 0 \\ 0 & 0 & F_{33} \end{pmatrix},\tag{12}$$

Specifically, F_{21} characterizes the shear deformation when the tension is in the oblique direction of mesogen alignment (He et al., 2020), as revealed from the experimental pictures in Fig. 1. F_{22} is the prescribed external loading. Also, the materials are assumed to be incompressible, resulting in $\det(F) = 1$. Note, this does not imply that $F_{11} \neq F_{33}$ when the deformation of transversely isotropic LCEs occurs in the X_1 - X_2 plane.

The governing differential equations of the developed constitutive model were solved numerically in MATLAB. The detailed simulation flow and time-integration algorithm is laid out in the Supplementary Materials (Section S6) and involves a set of initial conditions (no viscoelastic memory, an initial order parameter, and director orientation), a discretization in time of the mixed traction and deformation boundary conditions, and a time integration algorithm to march the simulation forward and satisfy the linear momentum balance. Specifically, at a given time step, the microscale directional angle of mesogen alignment, θ , in the current configuration is $\theta = \arctan(n_1/n_2)$. The macroscale shear angle, α , of the LCE sample is $\alpha = -\arctan(F_{21}/F_{11})$.

The experimental stress–strain relationships and the measured sample shear angles α are presented in Fig. 6a and Fig. 6b as dots. It is prominent to observe that the initial slopes of the stress–strain curves, which represent the material's elastic moduli, change significantly with the θ_0 value. The moduli are largest when stress is applied in the direction of the mesogen alignment and the lowest when they are perpendicular. The directional moduli of LCE samples at 0.01 s $^{-1}$ were used to determine the mapping function $f(\theta_0)$ in Eq. 4. Based on the mechanics of transversely isotropic lamina, the following expression is adopted in this study:

$$f(\theta_0) = \frac{1}{1 + e^{(\theta_0 - \pi/4)\beta_0}},\tag{13}$$

where β_0 is a fitting parameter. By fitting with the experimental data, it is determined to be 8 (Supplementary Materials, Section S7). This function allows initial nematic director orientations that span from 0 to $\pi/2$ radians, angles outside of this range are adjusted assuming biaxial symmetry.

The experimental results of stress–strain relationships in both uniaxial tension and compression across six decades of strain rate $(0.01-1600~\text{s}^{-1})$ are used to determine all other model parameters, such as the amount of non-equilibrium branches and their relaxation times. Detailed procedures for the parameter identification are further discussed in detail in the Supplementary Materials (Section S8). All the prescribed model parameters are detailed in Supplementary Materials (Section S9).

The uniaxial tension stress-strain curves with different initial nematic directors and loading rates are respectively compared in Fig. 6

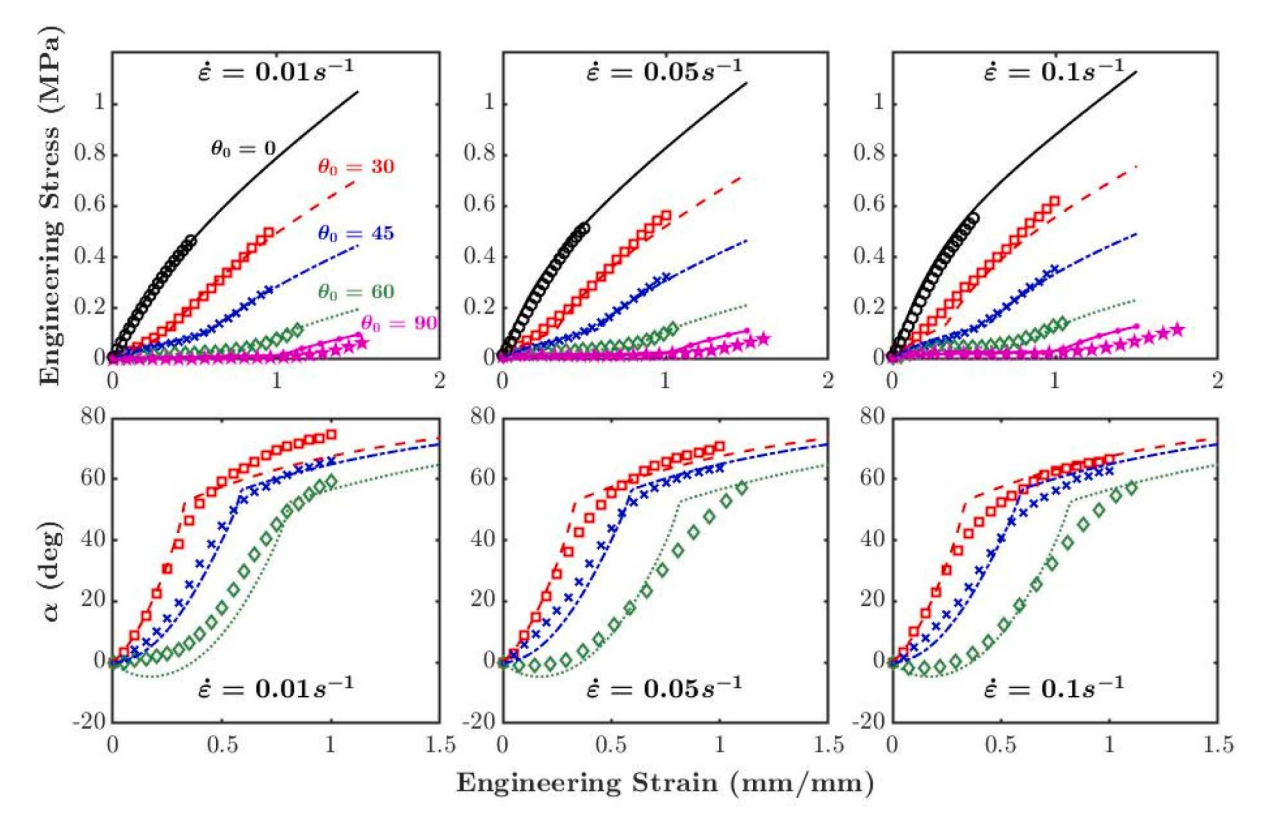


Fig. 6. Uniaxial tension experimental results (scatter) compared to model predictions (curves) for strain rates at different initial nematic directors. The first row displays the engineering stress versus engineering strain. The second row of plots displays the evolution of sample shear angle, *α*, as a function of engineering strain.

and Fig. S4 (Supplementary Materials, Section S10). As shown in these figures, when using seven Maxwell branches, the developed model closely captures all the experimental results with the three tested strain rates (0.01, 0.05, and 0.1 s⁻¹) in tension and the five different initial nematic directors (0°, 30°, 45°, 60°, 90°). The comparison with the experimental stress–strain data in uniaxial compression will be presented in the next section. The performance of our model in relation to the various initial nematic directors is mainly attributed to the neoclassical branch and Eq. (13), where the shear moduli of each Maxwell branch depend on θ_0 . The different strain rates are captured through the time relaxation constants of the Maxwell branch.

Fig. 6 reveals how soft elasticity is related to the micromechanics of LCEs. First, when the monodomain LCEs are stretched at a quasi-static loading rate in a direction oblique or perpendicular to the initial mesogen alignment, the stress initially increases slowly (soft elasticity as the mesogens reorient) and then rises sharply after reaching a critical strain level. Second, the extent of the soft elastic region, or the strain that marks a notable increase in stiffness, varies among samples with different initial nematic director orientations. For example, when θ_0 = 30° , this critical strain is ~ 0.3 , while it increases to ~ 1 for the $\theta_0 = 90^{\circ}$ sample. Third, the sample shear angle, α , of different LCE samples initially increases quickly with the external loading and then asymptotes roughly at the same critical strain. The overall increment of α is slower for the LCE samples with a higher θ_0 value. When the critical strain for soft elasticity is reached, the increase in shear angle is saturated. When $\theta_0 = 60^{\circ}$, the shear angle α is observed to first decrease slightly to a negative value and then increase. Note that in the theoretical model, all the predictions on shear angle converge to 90° at a sufficiently high strain level, which means the mesogens would align perfectly in the loading direction. However, this is not likely to occur in actual LCEs samples due to the exclusion effects of polymer chains (Rubinstein and Colby, 2003).

To further reveal the mechanisms behind the experimental observations, the evolution of the macroscopic stress–strain relationships at

the $0.01 \, \mathrm{s}^{-1}$ loading rate and the evolutions of microscale parameters, S and θ , are shown in Fig. 7. It is observed that the duration of the initial soft elasticity of the LCE samples depends on the extent of microscale mesogen rotation. The termination of soft elasticity for each sample roughly corresponds to the strain levels of the full rotation of mesogens (when θ reaches zero). Once fully rotated, any further stretching of the LCEs stretch and align the molecular chains. Therefore, the samples exhibit a higher stiffness and rapid increase of stress. On the other hand, the asymptotic behaviors of the shear angle indicate that the anisotropic conformational tensor in the neo-classical model has evolved fully into a diagonal matrix, which occurs when the nematic director is parallel to the external loading.

The evolutions of S in Fig. 7c suggest that the mesogen order parameter only changes notably after the nematic director is aligned with the loading direction. This is because the relaxation timescales of mesogen alignment, τ_S , is much larger than the nematic director reorientation timescale, τ_n , as revealed in the FTIR measurements (Luo, 2021). In other words, when the monodomain LCE is deformed, the nematic director evolves much quicker than the nematic order parameter. Therefore, at the early stage of soft elasticity, most of the energy is consumed to reorient the nematic director.

Both experimental results and model predictions also show the rate-dependent behaviors of monodomain LCEs. Since the constitutive model consists of two major components that physically represent the reorganization of the mesogen state (neo-classic branch) and the background network viscosity (Maxwell branches), it is intriguing to explore how these two parts contribute to the overall mechanical responses. In Fig. 8a and 8b, the overall stress responses of $\theta_0=0$ and 60° samples in both experiment and model predictions are plotted. In Fig. 8c and 8d, the corresponding stress response is split into two parts in the neo-classic branch and the Maxwell branches. The loading rate spans from 0.01 s $^{-1}$ to $0.1~{\rm s}^{-1}$.

It is observed that when the mesogens are initially parallel to the external tension ($\theta_0 = 0^{\circ}$), the rate differences of the overall stress

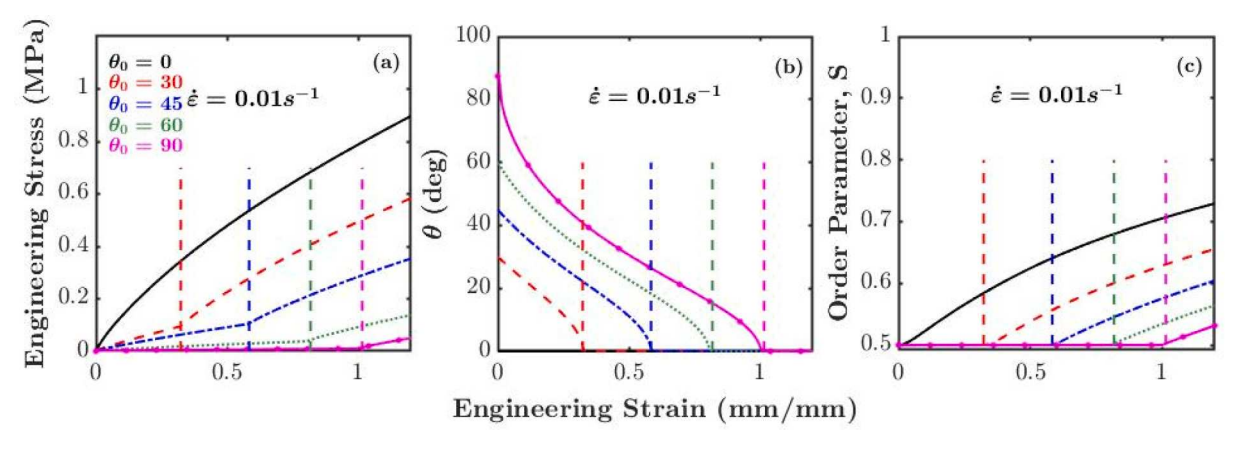


Fig. 7. Uniaxial tension predictions with a strain rate of $0.01 \, \mathrm{s}^{-1}$ at various initial nematic director orientations. (a) The engineering stress–strain relationships. The vertical dashed lines mark the end of soft elasticity, which are the critical strain levels. (b) The predicted evolutions of the nematic director. (c) The evolution of the nematic order parameter versus engineering strain.

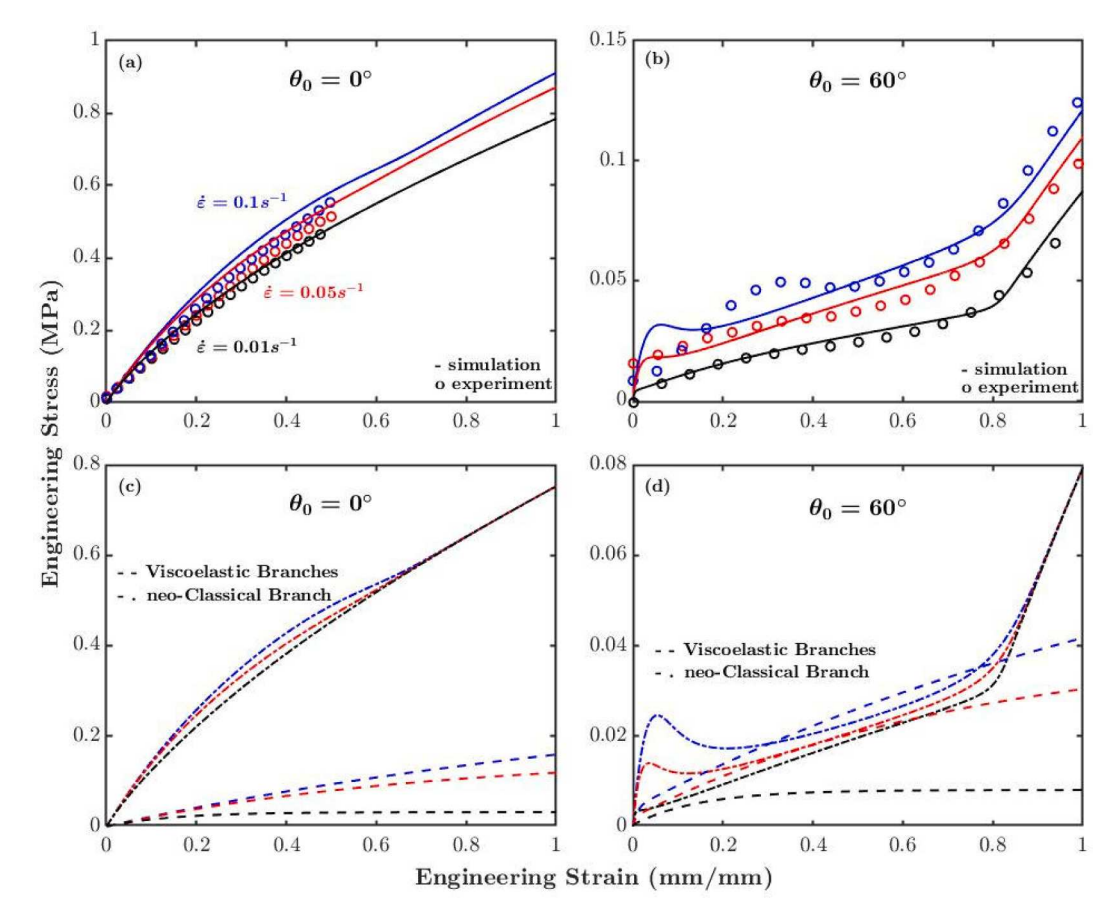


Fig. 8. (a) & (b) Stress–strain relationships in uniaxial tension experiments (circles) compared to the model predictions (solid lines) for varying strain rates with the same initial nematic directors. Each plot shows the results of the three tested strain rates for the same initial nematic director. (c) & (d) The contributions to stress responses from the viscoelastic (Maxwell elements: dashed) and neo-classic branches of the constitutive model.

responses of the LCE sample are less significant. Even though viscoelastic differences exist from the Maxwell branches, the neo-classic branch dominates the stress responses at these lower rates. For example, at the terminal strain of one, the peak stress of the neo-classic branch (~0.78 MPa) is nearly four times that in the Maxwell branches. The slight difference seen in the responses of the neo-classic branch is contributed to the evolution of the mesogen order parameter. Conversely, the LCE sample with $\theta_0=60^\circ$ exhibits more balanced contributions from both sets of branches, leading to a compounded rate

dependency in the overall stress–strain relationships. This comparison reveals the effect of the initial nematic director orientation relative to the constitutive balances between the background network viscoelasticity and intrinsic responses of mesogens.

The model predictions in Fig. 8d also suggest that when $\theta_0=60^\circ$, there is an initial mechanical instability of the neo-Classical branch wherein that branch of the model is at first very stiff but then suddenly softens before eventually stiffening again. This instability occurs in a more pronounced effect at higher strain rates. A similar phenomenon

was observed in a recent study by Wang et al. (Wang et al., 2022). To understand the mechanics of this instability, parametric studies are performed using the developed model to examine the mesoscopic behavior of LCEs at a higher strain rate in tension. In Fig. 9a through Fig. 9c, the overall stress responses of monodomain LCE samples at $1\,\mathrm{s}^{-1}$ to $100\,\mathrm{s}^{-1}$ are compared with different initial nematic director orientations. The contributions of the neo-classical branch are compared in Fig. 9d through Fig. 9f. The corresponding evolutions of mesogen alignment degree and director are compared in Fig. 9g through Fig. 9i and Fig. 9j through Fig. 9l, respectively.

The instability results from the delayed mesogen rotation when the timescale of external loading is comparable to or faster than the relaxation time of nematic director rotation, τ_n . For example, at a loading rate of 1 s⁻¹, the rotation of the nematic director of the $\theta_0=90^\circ$ LCE sample does not occur instantaneously. The input mechanical energy does not go into the mesogen rotation at this loading time scale, and the material shows a high stiffness neo-classical branch at low strains. Later, the nematic director starts to rotate with continued external deformation, and the sample exhibits soft elasticity with a plateau in stress, primarily in the neo-classical branch. Recall that we model the director and order

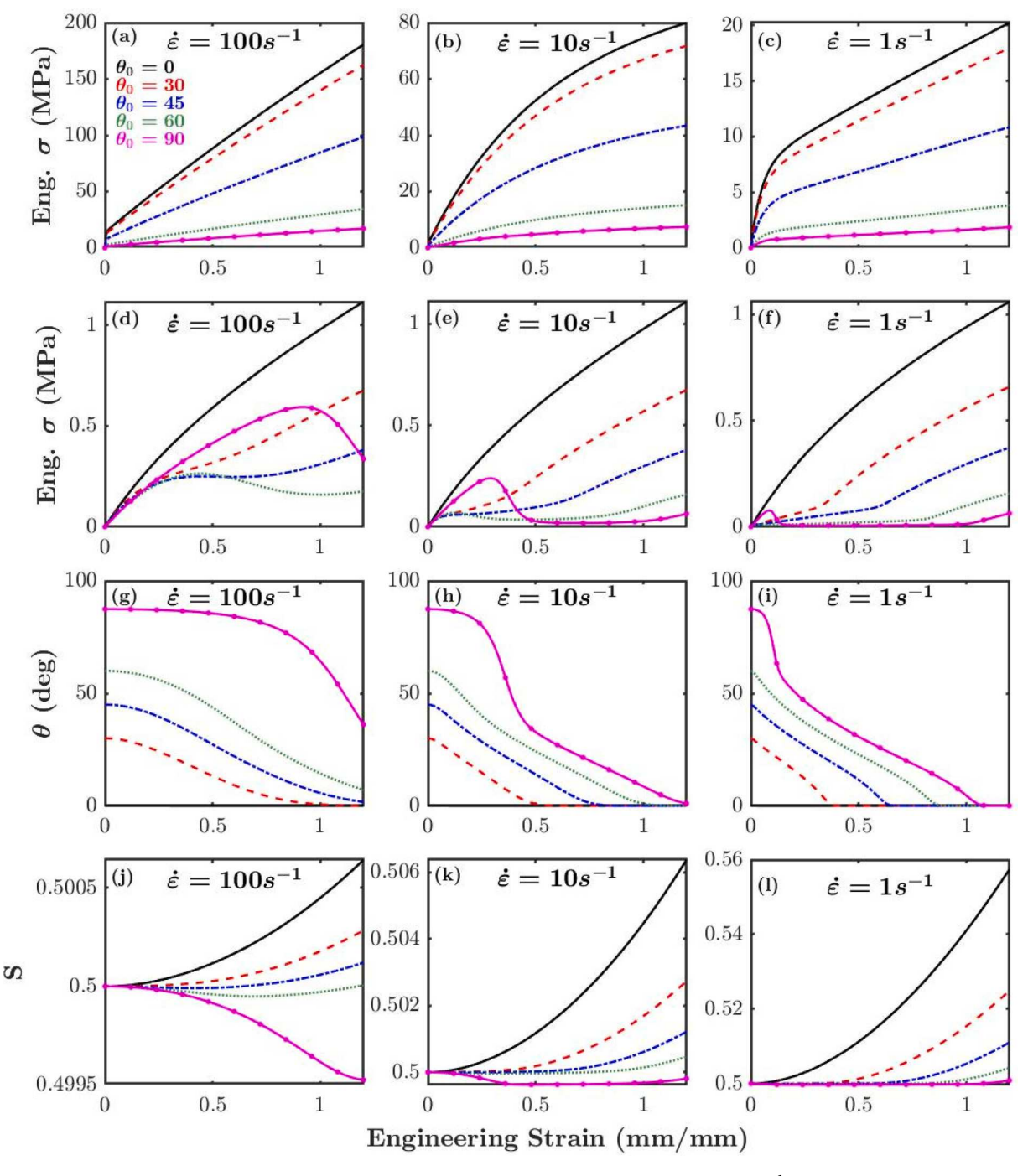


Fig. 9. Parametric studies on the uniaxial tension of monodomain LCEs at three different strain rates (1, 10, and $100 \, \text{s}^{-1}$) and five different initial nematic directors ($\theta_0 = 0^\circ$, 30° , 45° , 60° , and 90°). First row of plots (a, b, c): engineering stress–strain relationships. Second row of plots (d, e, f): the engineering stress contribution from the neo-classical branch. The third (g, h, i) and fourth (j, k, l) rows: the evolutions of the nematic director and mesogen order parameter, respectively. Higher strain rates delay the evolutions of the nematic director, which lead to a prolonged early stiffening in the overall stress response and a delay in the evolutions of the order parameter.

parameter time evolutions as proportional to the Helmholtz free energy density gradient with respect to these variables. So, as the sample continues to experience deformation, the driver for rotation or a change in order parameter increases. Eventually, the director rotates and cascades the order parameter to evolve. When the mesogens fully rotate, the stress response starts to increase dramatically. Both the mesogen order parameter and stress increase due to the stretch and alignment of polymer chains.

Further increasing the loading rate to $10 \, \mathrm{s^{-1}}$ and $100 \, \mathrm{s^{-1}}$ led to a more notable delay in mesogen rotation and a more prominent and broader initial peak stress in the neo-classical branch. LCE samples with oblique stretching directions relative to the mesogen alignment also start to show instability responses. The comparison between Fig. 9a through Fig. 9c and Fig. 9d through Fig. 9f suggests that the Maxwell branches dominate the overall stress response at the dynamic loading rates. For example, the highest stress of the neo-classic branch at 1.25 strain is $\sim 1 \, \mathrm{MPa}$, which is much smaller than the overall stress (20–200 MPa). Therefore, the initial peak stress or stiffening from the neo-classical branch is overwhelmed by the background viscoelastic branches at higher rates.

When the loading rate is at the dynamic region ($100 \, {\rm s}^{-1}$), the order parameter decreases initially before the mesogens start to rotate. This behavior is most visibly seen when $\theta_0 = 90^\circ$. Stretching the LCE samples in the normal direction relative to the mesogen alignment is equivalent to compressing the sample in the transverse direction (along the mesogen alignment). This deformation leads to the compression of polymer chains and a decrease in the mesogen order parameter. Similarly, the order parameter is also seen to decrease slightly for mesogens initially oriented at 60° (greater than 45°).

4.3. Quasi-static and dynamic compression behaviors

The developed model is further extended to study the uniaxial

compression behavior of monodomain LCEs, wherein the compression direction is parallel to the mesogen alignment with $\theta_0=0^\circ$. Unlike the uniaxial tension tests, the LCE sample with $\theta_0=0^\circ$ would exhibit the most mesogen rotation and soft elasticity during the uniaxial compression, the mesogens rotate to the horizontal direction, and θ increases to 90° .

The loading rate in the experiment increased from $0.01 \, \mathrm{s}^{-1}$ to $1600 \, \mathrm{s}^{-1}$. The overall stress–strain responses of the LCE samples are presented in Fig. 10a. The stress–strain curves at $1 \, \mathrm{s}^{-1}$ and $0.01 \, \mathrm{s}^{-1}$ are plotted separately in Fig. 10b to highlight the details at lower stress levels. In these two figures, the scatter plots are the experimental data, and the solid lines are the model predictions. Furthermore, the stress responses of the neo-classical branch are plotted in Fig. 10c. The associated evolutions of the mesogen order parameter, S, and the nematic director, n, are respectively plotted in Fig. 10d and Fig. 10e.

Overall, the developed constitutive model closely captures the experimental stress–strain data across five decades of loading rates. The mechanical response of monodomain LCEs in uniaxial compression is close to that revealed in uniaxial tension. The LCE samples exhibit significant rate-dependent responses with fundamentally different stress–strain relationships across different strain rates. At the quasistatic loading rate, the mesogens rotate immediately to absorb input energy primarily into mesogen rotation. This rotation leads to a stress plateau and soft-elastic behavior at low to moderate strains. The termination of soft elasticity is marked by the mesogens aligning in the perpendicular direction of compression near 0.5 strain at 0.01 s $^{-1}$, though this depends on initial nematic director orientation. After reaching this critical strain level, the mesogen order parameter increases notably due to the alignment of polymer chains, leading to a stiffer mechanical response of the LCE samples.

At a compressive engineering strain rate of $1~\rm s^{-1}$, the delay in mesogen rotation leads to a different mechanical response. The predictions in the figure suggest that the mesogens do not rotate till about

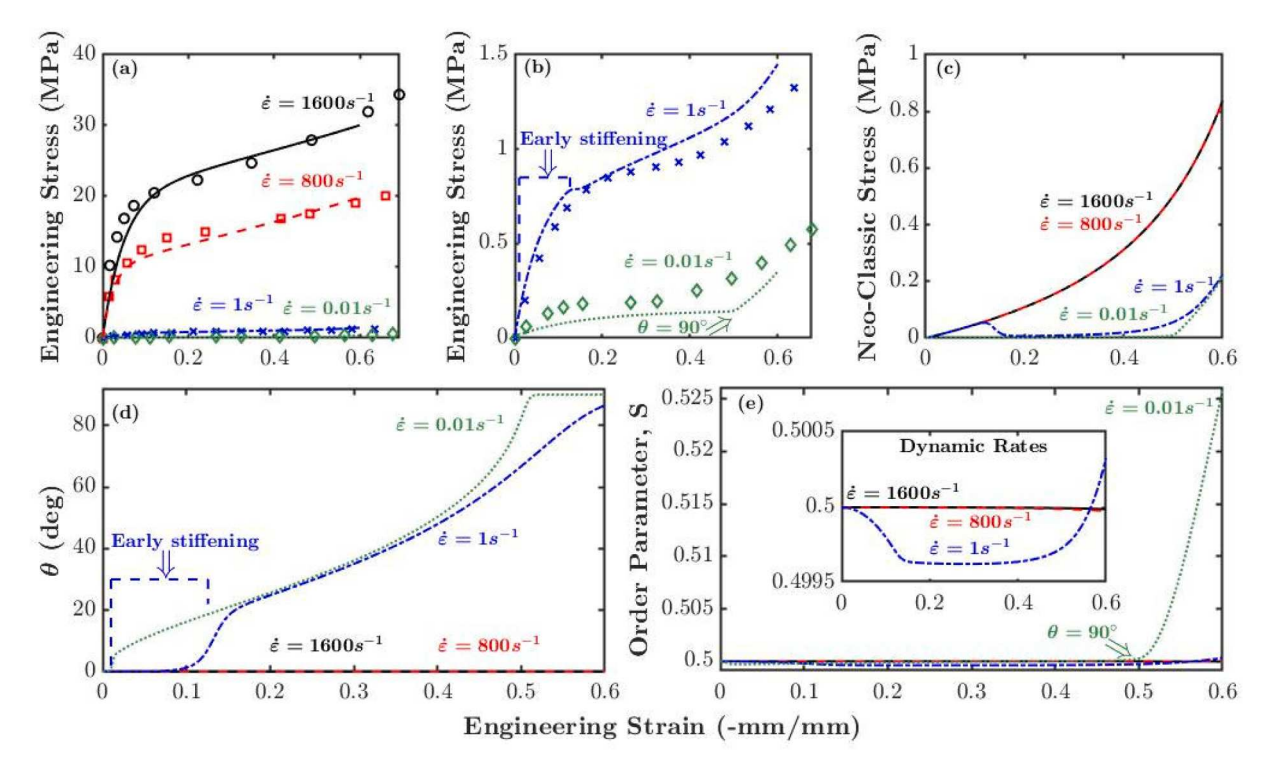


Fig. 10. Uniaxial compression behaviors of monodomain LCEs at quasi-static and dynamic loading rates. (a) Stress–strain relationships in the Kolsky bar and MTS compression tests (dots) and model predictions (curves). (b) Stress–strain relationships at slower rates (1 s^{-1} and 0.01 s^{-1}) for a more detailed view. (c) The comparison in stress responses of the neo-classic branch for the varying strain rates. (d) The evolution of the nematic director as a function of engineering strain. (e) The evolution of the mesogen order parameter, S, for the given strain rates. For dynamic rates, the order parameter does not change as dramatically compared to the equilibrium rate. These rates are plotted in a smaller window for a more detailed view.

0.1 compressive strain, and the neo-classic branch exhibits a significant stiffening in stress. However, the magnitude of the background viscoelasticity dominates the overall stress response. As shown in the Supplementary Material (Section S11), the neo-classic branch at 1 s⁻¹ loading rate is only responsible for \sim 4.1 % total energy absorption. Therefore, instead of a peak in stress, the early stiffening is drowned out by the background molecular matrix response. After \sim 0.1 compressive strain, the mesogens begin to rotate, resulting in a soft elastic.

Further increasing the loading rate to the dynamic region, the timescale for external compression deformation is much faster than the timescale of the mesogen rotation. For example, the simulation and experimental test only takes $\sim\!3.75\times10^{-4}$ s at $1600~s^{-1}$, which is much smaller than the nematic director reorientation timescale $(\tau_n\sim\!4\times10^{-2}$ s), found in Supplementary Material (Section S8). Therefore, the mesogen order parameter and nematic director are both unchanged. The stiffening behaviors are extended over the entire course of compression. LCEs at this dynamic rate behave much like a conventional viscoelastic transversely isotropic solid.

4.4. Parametric study on the stress-strain relationship and energy absorption

Due to the mesogen rotation, LCEs are an ideal material candidate for energy absorption. However, there is no existing study to quantitatively analyze their energy absorption capabilities, especially across various loading rates and directions. Here, the developed constitutive model is used to examine the energy absorption capabilities of monodomain LCEs with different initial nematic director orientations, terminal compressive strains, and strain rates.

For a quantitative analysis, we compare the stress responses of LCEs with those of i) an ideal energy absorber that would maintain a constant stress level during the deformation and ii) a conventional, incompressible viscoelastic elastomer with a constant equilibrium shear modulus during the compression. Using the developed constitutive model, the stress responses of LCEs with varying initial nematic director orientations are first predicted. The stress values are then normalized by that of the ideal absorber with the same amount of energy absorption (area under the stress–strain curve) with the same target compressive strain. As illustrated in Fig. 11a, after stress normalization, the response of the

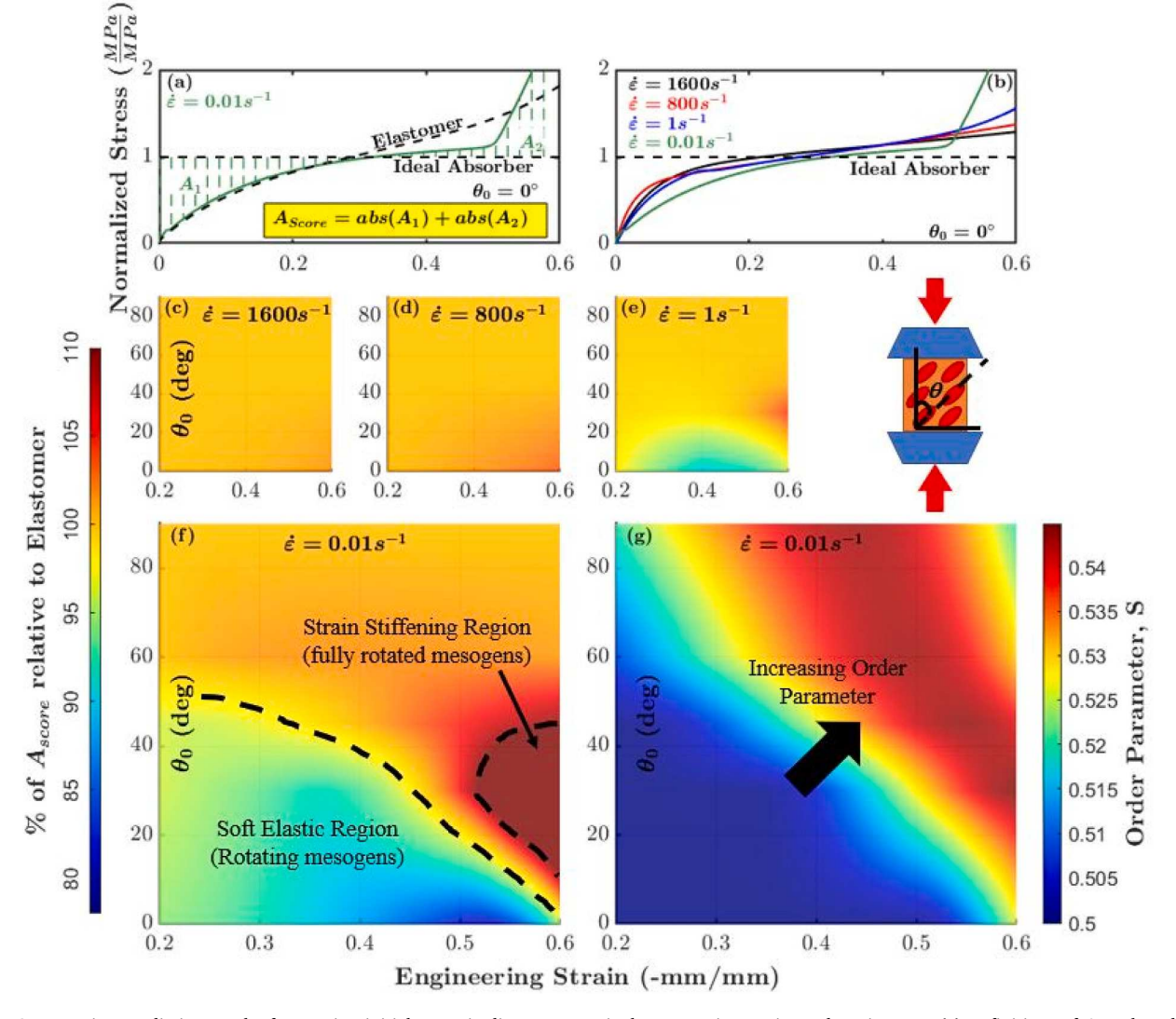


Fig. 11. Compression prediction results for varying initial nematic directors, terminal compressive strain, and strain rates. (a) Definitions of A_{score} based on the normalized stress–strain relationship. The A_{score} is a value that represents the magnitude of a sample's energy absorption relative to an ideal absorber. The A_{score} value suggests a closer energy absorption capability to an ideal absorber. (b) An example calculation for normalized stress of four different strain rates when $\theta_0 = 0^\circ$. The LCEs A_{score} as a percentage of a classical elastomer is predicted with varying initial nematic director orientations and terminal strain levels. The compressive strain rates are (c) 1600 s^{-1} , (d) 800 s^{-1} , (e) 1 s^{-1} , (f) and 0.01 s^{-1} , respectively. (g) The mesogen order parameter, S, at 0.01 s^{-1} with the same range of terminal strains and initial director orientations as that in plot (f).

ideal absorber is a horizontal line at 1 MPa/1 MPa. The response of the conventional viscoelastic elastomer is modeled as a Generalized Maxwell Model of order seven with the same relaxation times (exact values are found in Supplementary Materials, Section S8) as the LCEs. The only difference between the viscoelastic elastomer and the LCE is the addition of the neo-classical branch in the former. This allows for a precise comparison between the rotational mechanics of LCEs and a traditional rubber. The energy-absorption performance of LCE samples is characterized by the difference between their stress—strain curves and that of the ideal absorber using A_{score} (as defined in the figure) as a quantitative indicator. A smaller A_{score} results in greater energy-absorption characteristics.

An example of the normalized stress-strain relationships of monodomain LCEs with different loading rates is plotted in Fig. 11b, wherein compression is parallel to the initial mesogen alignment ($\theta_0 = 0^\circ$), and the target compression strain is 60 %. This initial nematic director orientation allows for full rotation of mesogens. However, mesogen rotation is only seen at rates of 1 $\rm s^{-1}$ and 0.01 $\rm s^{-1}$. This method was applied to all initial nematic director orientations between 0° and 90° in 1° increments, where the mechanistic effects of the initial orientation of the nematic director can be seen. At a glance, the mechanical response of LCEs at a dynamic loading rate (1600 s^{-1}) is closer to that of the ideal absorber. The corresponding energy absorption indicator A_{score} is 0.11 compared to 0.20 at the quasi-static loading rate of 0.01 s⁻¹. This implies that LCEs have better energy absorption properties at dynamic rates, where mesogen rotation does not exist. This result is counterintuitive to all prior literature promoting LCEs as an enhanced energy absorber. However, the energy-absorption behaviors of LCEs depend not only on their strain rate but also on their terminal strain. Previously, we mentioned in Fig. 10b a critical strain level of 0.5 for quasi-static loading rates indicating full mesogen rotation at this strain. After this critical strain, the stress increases significantly due to the lack of mesogen rotation. This sharp stress increase contributes to the increasing A_{score} and poorer energy absorption results at these lower rates. As one will see, if A_{score} is calculated prior to, or at the critical strain level, the results are very different.

To further explore the energy-absorption performances of LCEs, the indicator A_{score} is parameterized by initial nematic director orientations, terminal compressive strain, and strain rates. The A_{score} is then normalized by the same viscoelastic solid and is plotted using contour maps in Fig. 11c through Fig. 11f. In these contour plots, poorer energy absorbance is correlated to higher percentages. It is observed that there is a stark contrast between the dynamic loading rates of $1600 \, \rm s^{-1}$ and $800 \, \rm s^{-1}$ (Fig. 11c and Fig. 11d) and the lower strain rates of $1 \, \rm s^{-1}$ and $0.01 \, \rm s^{-1}$ (Fig. 11e and Fig. 11f). At dynamic rates, the LCEs exhibited similar energy absorption characteristics to those of the viscoelastic solid at all terminal strain levels and initial orientations. This result is expected because the mesogens have negligible rotational and alignment effects at such high loading rates, leading to the absence of soft elasticity, as mentioned in prior sections. Thus, at very high rates LCEs absorb a similar amount of energy as a classical viscoelastic elastomer.

As rates slow towards $1 \, {\rm s}^{-1}$ and lower, the A_{score} is reduced because of the now present effects of soft elasticity and mesogen rotation. The distributions of A_{score} are non-uniform across all initial nematic director orientations and terminal strains. For example, at $0.01 \, {\rm s}^{-1}$, the low percentage of A_{score} values is observed with an initial nematic director orientation closer to 0° (parallel to the compressive loading) because it allows for more rotation of mesogens, resulting in a longer soft elastic phase. The decreasing percent of A_{score} accumulates until the strain reaches the critical strain marked by fully rotated mesogens. The lowest A_{score} value, or the highest energy absorbance, is observed at the corresponding critical strain. This strain level is related to the rate and initial orientation of the nematic director. Further increasing the terminal strain will lead to stiffening, resulting in a higher A_{score} and reduced energy absorption. Furthermore, each sample's order parameter, S, notably increases when the mesogens are fully rotated. As shown

in Fig. 11g, the order parameter is increasing everywhere except in the soft elastic region depicted in Fig. 11f. In conclusion, LCEs outperform conventional viscoelastic materials when they deform (1) less than their respective critical strain, (2) at rates generally lower than $1 \, \mathrm{s}^{-1}$, and (3) at initial nematic directors that allow for mesogen rotation.

5. Conclusion

Overall, this study reveals the mechanisms of rate-dependent soft elasticity and mechanical energy absorption behaviors of nematic LCEs using an integrated experimental-theoretical approach. A thermodynamically consistent, nonlinear hyper-viscoelastic constitutive model was developed, which links the real-time evolution of mesogen organization (nematic director orientation and its degree of order) and finitestrain viscoelasticity to the overall mechanical response of LCEs under uniaxial tension and compression across six decades of strain rates. The major parameters of mesogen alignment and reorientation timescales are experimentally determined using FTIR measurements. The developed constitutive model is shown to closely capture the quasi-static and dynamic datasets in both tension and compression. The mechanical responses of LCEs are shown to strongly depend on the extent to which the external loading alters the mesogen organization, i.e., the mesogen orientation and alignment degree. Specifically, at quasi-static loading rates, the mesogens can effectively rotate to dissipate energy; the materials therefore exhibit soft elastic behaviors at the early stages of deformation. The mesogen alignment degree, however, does not change notably until the mesogens fully rotate to align with the external loading. This also marks the end of soft elasticity; further loading of the LCEs lead to a stiff mechanical response and increase in mesogen order parameter. When the external loading rate increases to a magnitude comparable to the timescale of mesogen rotation, a delay in mesogen rotation is present, leading to an initial stiffening effect in the overall stress-strain relationship of LCEs. Further increasing the loading rate to the dynamic region results in negligible mesogen rotation and soft elasticity behaviors during the deformation; LCEs behave much like conventional viscoelastic solids. Overall, this paper presents the first combined experimental and theoretical study on the soft elasticity and energy absorption behavior of LCEs across six decades of loading rates. It establishes the connections between external loading conditions, mesogen organization, and overall mechanical responses. It also defines the particular loading conditions where LCEs outperform conventional elastomers, which is critical for the future design of exciting applications

CRediT authorship contribution statement

Christopher Chung: Formal analysis, Investigation, Methodology, Software, Visualization, Writing – original draft, Data curation. Chaoqian Luo: Investigation, Validation. Christopher M. Yakacki: Formal analysis, Investigation, Methodology, Software, Visualization, Writing – original draft, Data curation. Bo Song: Data curation, Formal analysis, Investigation, Validation. Kevin Long: Conceptualization, Funding acquisition, Methodology, Validation, Writing – review & editing. Kai Yu: Conceptualization, Funding acquisition, Investigation, Methodology, Supervision, Validation, Writing – review & editing.

Declaration of competing interest

The authors declare the following financial interests/personal relationships which may be considered as potential competing interests: Kai Yu reports financial support was provided by National Science Foundation. Kai Yu, Kevin Long reports financial support was provided by Department of Energy.

Data availability

Data will be made available on request.

Acknowledgments

K.Y. acknowledges support from the National Science Foundation (CAREER Award CMMI-2046611). This work was supported by the Laboratory Directed Research and Development program at Sandia National Laboratories, a multi-mission laboratory managed and operated by National Technology and Engineering Solutions of Sandia LLC, a wholly owned subsidiary of Honeywell International Inc. for the U.S. Department of Energy's National Nuclear Security Administration under contract DE-NA0003525. This paper describes objective technical results and analysis. Any subjective views or opinions that might be expressed in the paper do not necessarily represent the views of the U.S. Department of Energy or the United States Government.

Appendix A. Supplementary data

Supplementary data to this article can be found online at https://doi.org/10.1016/j.ijsolstr.2024.112712.

References

- Aksenov, V., et al., 2007. FTIR spectroscopy of smectic elastomer films under lateral strain. Liq. Cryst. 34 (1), 87–94.
- Anglaret, E., et al., 2005. Molecular orientation in liquid crystal elastomers. Macromolecules 38 (11), 4799–4810.
- Azoug, A., et al., 2016. Viscoelasticity of the polydomain-monodomain transition in main-chain liquid crystal elastomers. Polymer 98, 165–171.
- Barnes, M., Verduzco, R., 2019. Direct shape programming of liquid crystal elastomers. Soft Matter 15 (5), 870–879.
- Bladon, P., Terentjev, E.M., Warner, M., 1993. Transitions and instabilities in liquidcrystal elastomers. Phys. Rev. E 47 (6), R3838–R3840.
- Bladon, P., Terentjev, E.M., Warner, M., 1994. Deformation-induced orientational transitions in liquid-crystals elastomer. J. Phys. II 4 (1), 75–91.
- Brand, H.R., Pleiner, H., 1994. Electrohydrodynamics of nematic liquid crystalline elastomers. Physica A 208 (3–4), 359–372.
- Cesana, P., Desimone, A., 2009. Strain-order coupling in nematic elastomers: equilibrium configurations. Math. Models Methods Appl. Sci. 19 (4), 601–630.
- Christensen, R., Theory of viscoelasticity: an introduction. 2012: Elsevier.
- Clarke, S., et al., 2001. Anomalous viscoelastic response of nematic elastomers. Phys. Rev. Lett. 86 (18), 4044.
- Conti, S., DeSimone, A., Dolzmann, G., 2002. Soft elastic response of stretched sheets of nematic elastomers: a numerical study. J. Mech. Phys. Solids 50 (7), 1431–1451.
- Conti, S., DeSimone, A., Dolzmann, G., 2002. Semisoft elasticity and director reorientation in stretched sheets of nematic elastomers. Phys. Rev. E 66 (6).
- Fried, E., Sellers, S., 2005. Orientational order and finite strain in nematic elastomers. J. Chem. Phys. 123 (4).
- Gharde, R.A., et al., 2015. Spectroscopic and thermo–mechanical studies of liquid crystal elastomer. Key Eng. Mater., Trans Tech Publications Ltd. 659, 495–499.
- Graewert, M.A., Svergun, D.I., 2013. Impact and progress in small and wide angle X-ray scattering (SAXS and WAXS). Curr. Opin. Struct. Biol. 23 (5), 748–754.
- Hanzon, D., et al., 2018. Adaptable liquid crystal elastomers with transesterificationbased bond exchange reactions. Soft Matter.
- Harada, M., et al., 2013. In-situ analysis of the structural formation process of liquid-crystalline epoxy thermosets by simultaneous SAXS/WAXS measurements using synchrotron radiation. Polym. J. 45 (1), 43–49.

- He, X., et al., 2020. Uniaxial tension of a nematic elastomer with inclined mesogens. Extreme Mech. Lett. 40, 100936.
- Holzapfel, G.A., 2002. Nonlinear solid mechanics: a continuum approach for engineering science. Meccanica 37 (4), 489–490.
- Kotikian, A., et al., 2018. 3D printing of liquid crystal elastomeric actuators with spatially programed nematic order. Adv. Mater. 30 (10), 17061641–17061646.
- Li, Y., et al., 2021. Remotely controlled, reversible, on-demand assembly and reconfiguration of 3D mesostructures via liquid crystal elastomer platforms. ACS Appl. Mater. Interfaces 13 (7), 8929–8939.
- Linares, C.P.M., et al., 2020. The effect of alignment on the rate-dependent behavior of a main-chain liquid crystal elastomer. Soft Matter 16 (38), 8782–8798.
- Luo, C., et al., 2021. Real-time alignment and reorientation of polymer chains in liquid crystal elastomers. ACS Appl. Mater. Interfaces 14 (1), 1961–1972.
- Mistry, D., et al., 2021. Soft elasticity optimises dissipation in 3D-printed liquid crystal elastomers. Nat. Commun. 12 (1), 1–10.
- Murthy, N.S., Minor, H., 1990. General procedure for evaluating amorphous scattering and crystallinity from X-ray diffraction scans of semicrystalline polymers. Polymer 31 (6), 996–1002.
- Olmsted, P.D., 1994. Rotational invariance and goldstone modes in nematic elastomers and gels. J. Phys. II 4 (12), 2215–2230.
- Reese, S., Govindjee, S., 1998. A theory of finite viscoelasticity and numerical aspects. Int. J. Solids Struct. 35 (26–27), 3455–3482.
- Rubinstein, M., Colby, R.H., 2003. Polymer Physics, Vol. 23. Oxford University Press, New York.
- Saed, M.O., et al., 2016. Synthesis of programmable main-chain liquid-crystalline elastomers using a two-stage thiol-acrylate reaction. JoVE (J. Vis. Exp.) 107, e53546.
- Saed, M.O., et al., 2017. High strain actuation liquid crystal elastomers via modulation of mesophase structure. Soft Matter 13 (41), 7537–7547.
- Saed, M.O., et al., 2017. Thiol-acrylate main-chain liquid-crystalline elastomers with tunable thermomechanical properties and actuation strain. J. Polym. Sci. B 55 (2), 157–168.
- Shaha, R.K., et al., 2020. Biocompatible liquid-crystal elastomers mimic the intervertebral disc. J. Mech. Behav. Biomed. Mater. 107, 103757.
- Tammer, M., et al., 2005. FTIR-Spectroscopy on Segmental Reorientation of a Nematic Elastomer under External Mechanical Fields. Macromol. Chem. Phys. 206 (7), 709, 714
- Terentjev, E., et al., 2003. Liquid crystalline elastomers: dynamics and relaxation of microstructure. Philos. Trans. R. Soc. Lond. Series A: Math. Phys. Eng. Sci. 1805 (361), 653–664.
- Terentjev, E., Warner, M., 2001. Linear hydrodynamics and viscoelasticity of nematic elastomers. Eur. Phys. J. E 4, 343–353.
- Thomsen, D.L., et al., 2001. Liquid crystal elastomers with mechanical properties of a muscle. Macromolecules 34 (17), 5868–5875.
- Traugutt, N., et al., 2017. Liquid-crystal order during synthesis affects main-chain liquid-crystal elastomer behavior. Soft Matter 13 (39), 7013–7025.
- Traugutt, N.A., et al., 2020. Liquid-crystal-elastomer-based dissipative structures by digital light processing 3D printing. Adv. Mater. 32 (28), 2000797.
- Tsai, S.W., Hahn, H.T. 2018. Introduction to Composite Materials: Routledge.
- Verwey, G., Warner, M., Terentjev, E., 1996. Elastic instability and stripe domains in liquid crystalline elastomers. J. Phys. II 6 (9), 1273–1290.
- Wang, Z., et al., 2022. A nonlinear viscoelasticity theory for nematic liquid crystal elastomers. J. Mech. Phys. Solids 163, 104829.
- Warner, M., Terentjev, E.M., 2007. Liquid Crystal Elastomers, Vol. 120. Oxford University Press.
- Warner, M., Gelling, K.P., Vilgis, T.A., 1988. Theory of Nematic Networks. J. Chem. Phys. 88 (6), 4008–4013.
- Warner, M., Terentjev, E.M., 2003. Liquid Crystal Elastomers. Oxford University Press, Oxford: New York.
- Zhang, Y., et al., 2019. Continuum mechanical modeling of liquid crystal elastomers as dissipative ordered solids. J. Mech. Phys. Solids 126, 285–303.
- Zhang, Y., Zhang, Z., Huo, Y., 2020. Nucleation and critical conditions for stripe domains in monodomain nematic elastomer sheets under uniaxial loading. J. Mech. Phys. Solids 144, 104110.
- Zhu, W., Shelley, M., Palffy-Muhoray, P., 2011. Modeling and simulation of liquid-crystal elastomers. Phys. Rev. E 83 (5), 051703.
- Zubarev, E.R., et al., 1999. Monodomain liquid crystalline networks: reorientation mechanism from uniform to stripe domains. Liq. Cryst. 26 (10), 1531–1540.